Ultracold atoms in multiple radio-frequency dressed adiabatic potentials

T. L. Harte,[1] E. Bentine,[1] K. Luksch,[1] A. J. Barker,[1] D. Trypogeorgos,[2] B. Yuen,[1] and C. J. Foot[1,*]

[1]*Clarendon Laboratory, University of Oxford, Oxford OX1 3PU, United Kingdom*

[2]*Joint Quantum Institute, University of Maryland and National Institute of Standards and Technology, College Park, Maryland 20742, USA*

(Received 31 August 2017; published 16 January 2018)

We present the first experimental demonstration of a multiple radio-frequency dressed potential for the configurable magnetic confinement of ultracold atoms. We load cold ^{87}Rb atoms into a double-well potential with an adjustable barrier height, formed by three radio-frequencies applied to atoms in a static quadrupole magnetic field. Our multiple radio-frequency approach gives precise control over the double-well characteristics, including the depth of individual wells and the height of the barrier, and enables reliable transfer of atoms between the available trapping geometries. We characterize the multiple radio-frequency dressed system using radio-frequency spectroscopy, finding good agreement with the eigenvalues numerically calculated using Floquet theory. This method creates trapping potentials that can be reconfigured by changing the amplitudes, polarizations, and frequencies of the applied dressing fields and easily extended with additional dressing frequencies.

DOI: 10.1103/PhysRevA.97.013616

I. INTRODUCTION

Our understanding of quantum systems has been shaped by the ability to study ultracold atoms in a variety of trapping geometries. These range from regular potentials such as lattices [1], waveguides [2], rings [3,4], and box traps [5,6] to more arbitrary configurations such as tunnel junctions [7] and disordered potentials [8]. Such traps are often implemented using optical methods, exploiting their versatility in spite of drawbacks such as unwanted corrugations from fringes, sensitivity to alignment, and off-resonant scattering processes that require large detunings and associated optical powers.

The application of a radio-frequency (RF) field to a static magnetic trap dramatically changes the character of the confinement [9,10], providing additional parameters to control the potential while retaining the advantages over optical dipole force traps. A single RF applied using an atom chip [11] has been used to coherently split a one-dimensional (1D) quantum gas [12], a technique since used to shed light on the nature of thermalization in near-integrable 1D quantum systems [13]. RF 'dressed' adiabatic potentials (APs) have also been employed to probe 2D gases [14,15]. Ring traps can be implemented by time averaging [16,17] or by the addition of an optical dipole potential [18] and are used to study superflow or for matter-wave Sagnac interferometry [2]. The introduction of a multiple radio-frequency (MRF) field provides an additional means by which to shape these potentials [19], further increasing the versatility of magnetic traps.

In this work we demonstrate MRF APs for the first time, creating a highly configurable double-well potential with three radio-frequencies. Dynamic control over these potentials, which take the form of two parallel sheets, can be achieved by manipulating the RF polarization and amplitude or properties of the underlying static field [2,20,21]. These traps are intrinsically state and species selective [19,22,23], with demonstrably low heating rates when created using macroscopic coils located a few centimeters from the atoms [14]. Magnetic double-well potentials have previously been demonstrated using a single RF on an atom chip [12,20] and by time-averaging either a bare magnetic trap [24,25] or an AP [16,17]; our MRF method builds upon these works to offer increased tunability through independent control of the constituent dressing-field components. This double-well potential could be developed to investigate tunneling dynamics or cold-atom interferometry [12,26] between pairs of 2D sheets. As a natural extension, additional frequency components can be applied to produce lattices [19], continuous potentials, or wells connected to a reservoir [27].

Our discussion begins with an introduction to the theory of MRF dressed potentials in Sec. II, focusing on the experimentally demonstrated three-frequency field. In Sec. III we present our experimental results, exploring the manipulation of atoms in our MRF double-well potential. We describe the experimental apparatus and methods in Sec. III A and demonstrate precise control over the potential landscape in Sec. III B.

After a discussion of RF spectroscopy methods in Sec. III C, we use this technique to probe the MRF potential landscape and validate our theoretical model in Sec. III D. We conclude in Sec. IV by outlining the experimental possibilities arising with complex trapping geometries controlled by multiple RF fields.

II. ATOMS IN A MULTICOMPONENT RF FIELD

The dressed-atom picture of atom-radiation interaction [28,29] can be used to describe atoms trapped in optical, microwave [30,31], and RF fields [9]. An RF dressed adiabatic potential provides a trapping mechanism for cold atoms subjected to uniform RFs and inhomogeneous static magnetic fields [9,32]. We describe the theory of MRF dressed potentials in

*christopher.foot@physics.ox.ac.uk

two parts: Sec. II A presents the calculation of the quasienergy spectrum using Floquet theory, and Sec. II B describes the resulting potential surfaces and practical considerations of their implementation.

A. Atom-photon interactions

In this work we consider ^{87}Rb atoms in the $F = 1$ hyperfine ground state, originally confined in the static magnetic quadrupole field

$$\mathbf{B}_0(\mathbf{r}) = B'_q(x\hat{\mathbf{e}}_x + y\hat{\mathbf{e}}_y - 2z\hat{\mathbf{e}}_z), \tag{1}$$

with B'_q the radial quadrupole gradient and $\hat{\mathbf{e}}_x$, $\hat{\mathbf{e}}_y$, and $\hat{\mathbf{e}}_z$ the Cartesian unit vectors. This inhomogeneous field introduces a spatial dependence to the Zeeman splitting between hyperfine sublevels. We apply the homogeneous MRF dressing field

$$\mathbf{B}_{\mathrm{MRF}}(t) = \sum_j B_j \frac{\cos(\omega_j t + \phi_j)\hat{\mathbf{e}}_x - \kappa_j \sin(\omega_j t + \phi_j)\hat{\mathbf{e}}_y}{\sqrt{1+\kappa_j}}, \tag{2}$$

where B_j, ω_j, and ϕ_j are the amplitude, angular frequency, and relative phase of each frequency component, respectively. In our experimental implementation we use three RF components, $\omega_j = \omega_{1,2,3} = 2\pi \times (5,6,7) \times 0.6$ MHz, producing circularly polarized dressing fields for $\kappa_j = 1$ and linearly polarized fields for $\kappa_j = 0$. The following discussion describes either linear or circularly polarized RF fields, for which the dressed-atom Hamiltonian of the system reads

$$V = \sum_j \hbar\omega_j a_j^\dagger a_j + g_F \mu_B \mathbf{F}\cdot[\mathbf{B}_0(\mathbf{r}) + \mathbf{B}_{\mathrm{MRF}}], \tag{3}$$

where

$$\mathbf{F}\cdot\mathbf{B}_{\mathrm{MRF}} = \sum_j \mathscr{E}_j \left(\frac{\alpha_j}{\sqrt{2}}F_+ + \frac{\beta_j}{\sqrt{2}}F_- + \zeta_j F_z\right)a^\dagger + \mathrm{H.c.} \tag{4}$$

In this expression, $\mathbf{B}_{\mathrm{MRF}}(t)$ now describes the second quantized operator for the MRF field with mode densities $\mathscr{E}_j$ and amplitudes α_j, β_j, and ζ_j as defined in Eqs. (5) and (6). The Hermitian conjugate is indicated by H.c., while g_F denotes the Landé g factor and μ_B the Bohr magneton.

The first term in Eq. (3) accounts for the energy of the RFfield component j with angular frequency ω_j and the corresponding photon creation and annihilation operators $a_j^\dagger$ and a_j. The second term describes the interaction between the atomic spin $\mathbf{F}$, defined following the convention in Ref. [33], and the total magnetic field, comprising static and RF components with operators $\mathbf{B}_0(\mathbf{r})$ and $\mathbf{B}_{\mathrm{MRF}}(t)$, respectively.

The combined system of a magnetically confined atom, RF radiation, and the interaction between them can be intuitively described in the dressed-atom picture, as illustrated in Fig. 1 for a single- and triple-frequency field. In the absence of interactions with the RF field, the dressed eigenstates $|n_1,n_2,\ldots,m_F\rangle$ are the tensor products of the Fock states of each RF field $|n_j\rangle$ and the atomic Zeeman substates $|m_F\rangle$. These form a ladder of eigenenergies $g_F\mu_B m_F|\mathbf{B}_0| + \sum_j n_j\hbar\omega_j$ in which the three Zeeman substates are repeated with a spacing of ω_f, the highest common factor of RF photon frequencies ω_j. The interaction described by Eq. (4) drives transitions between dressed states, turning energy level crossings into avoided crossings.

While the dressed-atom picture provides an intuitive visualization of the RF dressing process, the large mean photon number of the RF field allows it to be represented classically by replacing $\mathscr{E}_j a_j^\dagger$ and $\mathscr{E}_j a_j$ with their mean field value $\frac{1}{2}B_j$. This is performed within the context of the interaction picture, in which $V \to U_{\mathrm{RF}}^\dagger V U_{\mathrm{RF}}$ and $|\psi\rangle \to U_{\mathrm{RF}}^\dagger|\psi\rangle$ with $U_{\mathrm{RF}} = \exp[i\sum_j a_j^\dagger a_j \omega_j t]$.

The RF field is decomposed into components parallel and perpendicular to a local axial vector $\hat{\mathbf{z}}'$, where $\mathbf{F}\cdot\mathbf{B}_0 = B_0 F_{z'}$. The parallel component is given by $\frac{1}{2}B_j\zeta_j\exp[i(\omega_j t + \phi_j)] + \mathrm{c.c.}$, where c.c. indicates the complex conjugate, with

$$\zeta_j(\mathbf{r}) = \frac{1}{\sqrt{1+\kappa_j}}(\sin\theta\cos\phi + i\kappa_j\sin\phi). \tag{5}$$

From the definition of the static quadrupole field, $\cos\theta = -2z(x^2+4z^2)^{-1/2}$ and $\cos\phi = [(x^2+4z^2)/(x^2+y^2+4z^2)]^{1/2}$. The anticlockwise- and clockwise-rotating components of the perpendicular field are $\frac{1}{2}B_j\alpha_j\exp[i(\omega_j t + \phi_j)] + \mathrm{c.c.}$ and $\frac{1}{2}B_j\beta_j\exp[i(\omega_j t+\phi_j)] + \mathrm{c.c.}$, respectively, with

$$\begin{aligned}\alpha_j(\mathbf{r}) &= \frac{1}{\sqrt{2+2\kappa_j}}(\cos\theta - i\sin\theta\sin\phi - \kappa_j\cos\phi),\\ \beta_j(\mathbf{r}) &= \frac{1}{\sqrt{2+2\kappa_j}}(\cos\theta + i\sin\theta\sin\phi + \kappa_j\cos\phi).\end{aligned} \tag{6}$$

In this basis the semiclassical version of the Hamiltonian presented as Eq. (3) becomes

$$\begin{aligned}V(t) = g_F\mu_B B_0 F_z + \frac{g_F\mu_B}{2}\sum_j\Bigg[&\left(\frac{\alpha_j}{\sqrt{2}}F_- + \frac{\beta_j}{\sqrt{2}}F_+ + \zeta_j F_z\right)B_j e^{i(\omega_j t+\phi_j)}\\ &+ \left(\frac{\alpha_j^*}{\sqrt{2}}F_+ + \frac{\beta_j^*}{\sqrt{2}}F_- + \zeta_j^* F_z\right)\\ &\times B_j e^{-i(\omega_j t+\phi_j)}\Bigg],\end{aligned} \tag{7}$$

which is periodic in time with period $T = 2\pi/\omega_f$. The coefficients α_j, β_j, and ζ_j give the projection of the field operator in the local circular basis, with $|\alpha_j|^2 + |\beta_j|^2 + |\zeta_j|^2 = 1$.

Using Floquet's theorem, the eigenstates of this time-periodic Hamiltonian, with period T, can be expressed in the form $|\psi(t)\rangle = \exp[iE't/\hbar]\,|\Psi(t)\rangle$, the product of a phase term and the time-periodic state vector $|\Psi(t)\rangle$, where $|\Psi(0)\rangle = |\Psi(T)\rangle$. Alternatively, one can write $|\psi(t)\rangle = U(t)\,|\psi(0)\rangle$, where $U(t)$ is the time evolution operator. We calculate U through numerical integration of the Schrödinger equation with the interaction Hamiltonian, Eq. (7). Comparing these two equations for $|\psi(t)\rangle$, we find $U(T)\,|\psi(0)\rangle = |\psi(T)\rangle = \exp[iE'T/\hbar]\,|\psi(0)\rangle$. The phases $E'T/\hbar$ can be associated with the energy of the dressed eigenstates of Eq. (3) at time T [34,35] such that the dressed-state eigenenergies modulo $\hbar\omega_f$ are given by the $2F+1$ eigenvalues of $(-i\hbar/T)\log U(T)$. These eigenenergies are illustrated in Fig. 1 for the three-RF example that we investigate experimentally.

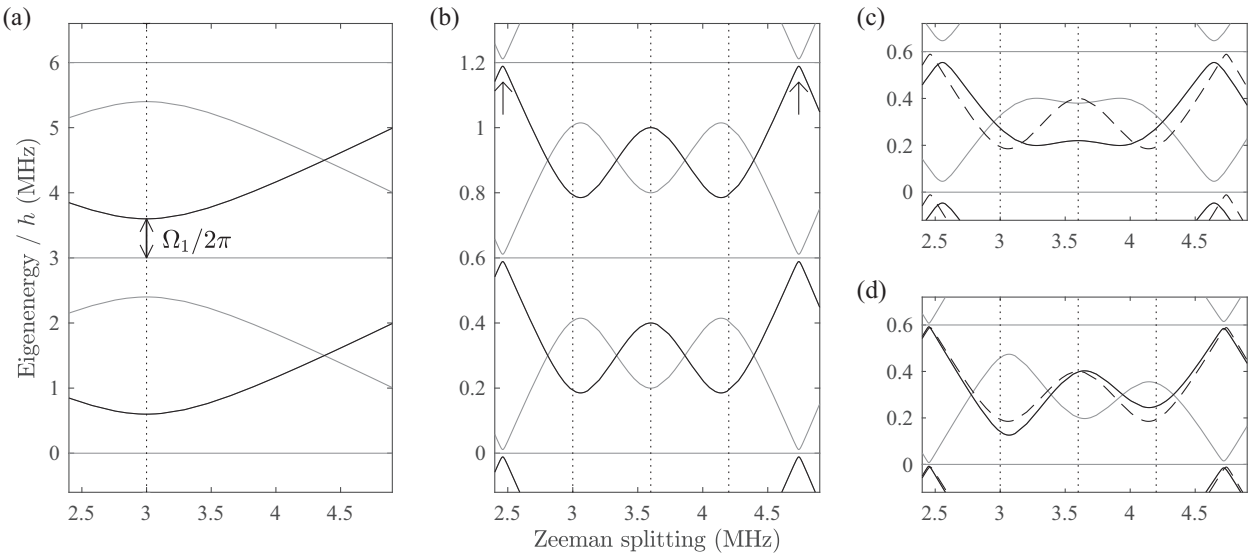

FIG. 1. (a) Eigenenergies of the dressed atomic states showing the avoided crossing that forms due to a single applied RF at ω_1 (dotted vertical line). Black lines show the trapping well for atoms in $|\widetilde{m}_F = 1\rangle$ with Rabi frequency Ω_1. Gray lines show the untrapped $|\widetilde{m}_F = 0, -1\rangle$ eigenenergies. (b) A three-component RF field forms a double well. The system periodicity is now defined by ω_f, the highest common factor of the RF components, with avoided crossings formed at the resonance of each RF component. The energies of the eigenstates at each resonance are shifted by the presence of the other RFfield components, translating the well minima in space. Weak avoided crossings are also formed by multiphoton couplings at integer values of $\hbar\omega_f$, indicated by arrows. (c) The potential can be deformed into a broad single well by increasing the amplitude of the middle field component. Solid and dashed lines show the potential for different barrier heights. (d) The relative amplitudes of the outermost RFs control the imbalance in well depth. Any combination of RF amplitudes can be used to shape the potential, for example, to mediate atom transport between the wells. Note that, for clarity, we omit effects of gravity in figures except where it serves an illustrative purpose.

B. Adiabatic potentials

The interaction $g_F \mu_B \mathbf{F} \cdot \mathbf{B}_{\mathrm{MRF}}$ couples the states to form avoided crossings at values of the static field for which the energy splitting $g_F \mu_B B_0$ is resonant with an integer multiple of $\hbar\omega_f$. When this interaction is sufficiently strong and the static field orientation varies sufficiently slowly with position, an atom traversing an avoided crossing can adiabatically follow this new eigenstate, labeled by the quantum number $\widetilde{m}_F$ [36].

In the case of a single applied RF with angular frequency ω_1 shown in Fig. 1(a), atoms trapped in $\widetilde{m}_F = 1$ experience a trapping potential $U_{AP}(\mathbf{r}) = \widetilde{m}_F \hbar \sqrt{\delta^2(\mathbf{r}) + \Omega_1^2(\mathbf{r})}$, where $\delta(\mathbf{r}) = |g_F \mu_B B_0(\mathbf{r})/\hbar| - \omega_1$ gives the angular frequency detuning of the RF from resonance and the Rabi frequency is determined by the applied RF amplitude and polarization.

The spatial variation of the static field amplitude $B_0(r)$ translates the detuning dependence of the potential to a spatial dependence, such that for the static quadrupole of Eq. (1) the resultant trapping potential forms an oblate spheroidal 'shell trap.' Atoms are trapped on the surface of this resonant spheroid, over which the spatial variation of the coupling strength is dictated by the RF polarization.

The Rabi frequency for a circularly polarized RF field is given by

$$\Omega_1 = \frac{g_F \mu_B B_1}{2\sqrt{2}\hbar}\left(1 \pm \frac{2z}{\sqrt{x^2 + y^2 + 4z^2}}\right), \tag{8}$$

with B_1 the magnetic field amplitude of the ω_1 RF field and x, y, and z Cartesian coordinates with their origin at the center of the quadrupole field. The sign of the second term depends on the handedness of the RF field polarization; in this work the handedness is chosen such that the coupling is maximized at the south pole of the resonant spheroid. For the case of an RF field linearly polarized in the xy plane the Rabi frequency instead takes the form

$$\Omega_1 = \frac{g_F \mu_B B_1}{2\hbar}\left(\frac{r_\perp^2 + 4z^2}{r_\perp^2 + r_\parallel^2 + 4z^2}\right)^{1/2}, \tag{9}$$

where $r_\parallel$ and $r_\perp$ describe the coordinates parallel and perpendicular to the polarization direction of the linear RF field. The resonant spheroid therefore has maximum coupling at points for which the parallel component is 0 and zero coupling at the points on the equator for which the perpendicular component is 0.

As illustrated in Fig. 1(b), this principle can be easily extended to the MRF case, in which the three first-order avoided crossings form two trapping wells separated by an antitrapping barrier for an atom in $\widetilde{m}_F = 1$. This results in trapping on two concentric spheroids forming a spatially extended double well in which the relative heights of the barrier and both wells are controlled by the three separate input RFs. Multiphoton interactions lead to cross-talk between these features, and the impact of the amplitude Ω_j of each avoided crossing on the properties of its neighbors is investigated experimentally in Secs. III B and III D. Also studied in Sec. III D is the effect of the relative phase ϕ_j between RF components; this alters the overall shape of the MRF waveform and thus influences the strength of nonlinear multiphoton processes that occur.

Adiabaticity constraints motivate the choice of parameters including the frequency separation, RF amplitudes,

and static field gradient. An atom moving at a constant velocity v through this spatially varying potential will remain trapped with a probability approximately given by the Landau-Zener (LZ) model: this states that $P_{\mathrm{LZ}} = (1 - \exp[-h\Omega^2/4g_F\mu_B\partial_t B_0(vt)])^2$, where the time derivative of the static field B_0 indicates the field gradient as experienced by the moving atom [19,37]. Minimizing the well spacing requires a dressing RF frequency separation comparable to the Rabi frequency of each RF component.

As the piecewise approach presented in Ref. [19] is invalid in this limit [38,39], Floquet theory is employed to calculate the MRF dressed-state eigenenergies. Numerical artifacts are removed by appropriate meshing over the range of magnetic field values considered, while an intuitive depiction of MRF dressing that uses the resolvent formalism to discard these artifacts is explored in Ref. [35].

III. EXPERIMENTAL IMPLEMENTATION OF THE MRF POTENTIALS

A. Trapping atoms in an adiabatic potential

In standard operation, we routinely produce BECs of 3.5×10^5 ^{87}Rb atoms in the $|F = 1, m_F = -1\rangle$ hyperfine state using a time-orbiting potential (TOP) trap [40], via an experimental sequence that we can truncate to load thermal atoms into an AP prior to a final stage of evaporation. The TOP is formed by applying a bias field, rotating at 7 kHz, to the static quadrupole field of Eq. (1). This bias field sweeps the quadrupole field in a horizontal circular orbit with a rotation radius given by $B_T/B_q^{'}$, with B_T the amplitude of the TOP field.

The TOP and dressing RF fields are generated by a coil array that surrounds the atoms, with an extent of a few centimeters. This array is illustrated in Fig. 2. The RF signals for each coil and frequency component are independently generated by direct digital synthesis [41]. This digital control over the amplitude and polarization of each dressing field component enables us to precisely sculpt the waveform and resultant potential as a function of time. The signals for each coil are combined using splitters [42] and amplified by 25-W amplifiers [43]. The RF coil array has a self-resonance of approximately 7 MHz such that, with a custom wide-band impedance match, we can confine atoms in APs with dressing frequencies in the range $2\pi \times 2.7$ to $2\pi \times 4.4$ MHz without additional amplification. Mixing processes in the amplifiers constrain us to use only combinations of dressing frequencies with a common fundamental ω_f, ensuring that the resulting intermodulation products are far detuned from transitions between dressed states such that we avoid losses.

We load a single-RF shell with thermal atoms as described in [17,21,44], combining the TOP field with dressing RF to produce a time-averaged adiabatic potential (TAAP) as illustrated in Figs. 2(b)– 2(e). The dressing RF is switched on while the TOP field satisfies $2\hbar\omega_1/g_F\mu_B > B_T > \hbar\omega_1/g_F\mu_B$ such that the TOP field sweeps the resonant spheroid in an orbit outside the location of the atom cloud. With an RF amplitude of the order of $\Omega_j = g_F\mu_B B_j/(\sqrt{2}\hbar) = 2\pi \times 400$ kHz at the south pole of the spheroid, decreasing B_T allows us to load the atoms into the TAAP formed at the lower of the two intersections of the spheroid with the rotation axis under the influence of gravity. The RF field is circularly polarized in the laboratory frame, with a handedness that maximizes the interaction strength at the bottom of the resonant spheroid. Using an additional weak field we then optionally perform forced RF evaporation to BEC in 2 s, exploiting the enhanced radial trap frequencies inherent to the TAAP. Reducing B_T to 0 subsequently loads atoms from the TAAP onto the lower surface of the shell. This reliably loads condensates of greater than 3×10^5 atoms into the shell trap with negligible heating.

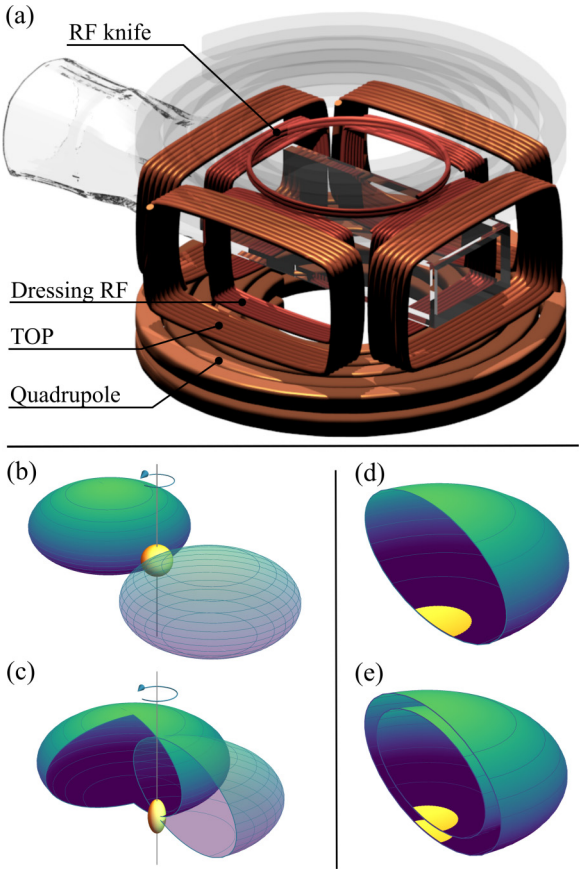

FIG. 2. (a) Our magnetic fields are generated by a coil array that surrounds the ultrahigh-vacuum glass cell. The racetrack coils are connected in pairs to generate orthogonal components of the rotating TOP and dressing RF fields. The single circular coil provides the RF knife used in evaporation and spectroscopy. Quadrupole gradients are applied using the large anti-Helmholtz coils located above and below the a.c. array. (b) Prior to loading the AP, the atoms are confined in the TOP. When the dressing RF is applied, the rotating bias field of amplitude B_T moves the resonant spheroid in a circular orbit. For $B_T > \hbar\omega_1/\mu_B g_F$ the shell orbits outside the atom cloud (yellow area). (c) Lowering B_T causes an intersection of spheroid and rotation axis, creating and loading the TAAP where RF evaporation can be performed. (d) $B_T \to 0$, loading atoms into the shell trap. (e) Applying three dressing RFs creates the double-shell potential.

B. Potential shaping and the double shell

This single-RF configuration forms the starting point for the MRF double-well potential, with atoms initially confined in the shell corresponding to either ω_1 or ω_3 and ultimately transferred into the combined $\omega_{1,2,3} = 2\pi \times (5,6,7) \times 0.6$ MHz

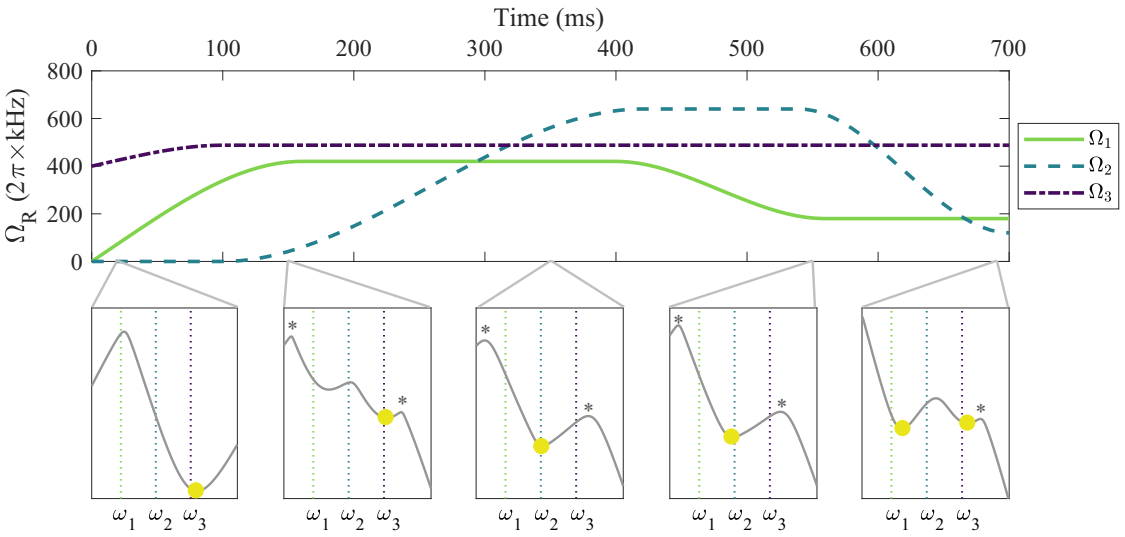

FIG. 3. Typical time sequence of the dressing RF amplitudes used to load a BEC into the double-shell configuration, where $\Omega_j = g_f \mu_B B_j/(\sqrt{2}\hbar)$ denote the constituent field amplitudes. The lower panels show the three-frequency potential (including gravity) at key times during this loading sequence, with dotted lines indicating the locations associated with the first-order resonances of the dressing frequencies, ω_1, ω_2, and ω_3. This illustrates the transformation into a three-frequency single well before the barrier is raised to split the cloud between the two wells. These experimental parameters avoid losses due to the second-order resonances indicated by stars in the panels above. The relative amplitudes of the RF components determine the final distribution of atoms between each well.

potential. In our apparatus the $2\pi \times 0.6$ MHz frequency difference between RF components maps to a spatial well separation of ~140 μm at a quadrupole gradient $B_q^{'} = 62.45$ G/cm, allowing the trapping wells to be clearly resolved with our low-resolution imaging system. The double-shell loading procedure is shown in Fig. 3 for the case of loading from a single shell at ω_3. We first ramp up Ω_1, which has a minimally perturbative effect on the potential near the atoms but establishes this resonance in preparation for the subsequent application of the field at ω_2. As shown in Fig. 1, the avoided crossing formed by ω_2 takes the form of an antitrapping barrier. As Ω_2 increases, the barrier is lowered and the MRF potential is flattened, rounded out, or tilted slightly according to the desired loading scheme and relative values of Ω_1, Ω_2, and Ω_3. To minimize any sudden changes in the width of the potential experienced by the atoms as the barrier is lowered, Ω_1 is held at an artificially high value and lowered to the value at which atoms can be transferred only once the barrier has been ramped down fully. Once atoms equilibrate within this new potential, we raise the barrier to separate the wells and complete the loading process. This method is illustrated in Fig. 3 for the RF ramps used to split a BEC between the two shells, and variants on this loading scheme were used in the remaining figures. The second-order resonances apparent in Fig. 3 place an upper limit of $\hbar\omega_f$ on the well depth; the combination of RF amplitudes and frequency separation is therefore chosen to complement the temperature of atoms loaded into the potential.

The final population imbalance between the wells is influenced by the relative amplitudes of each RF component during the ramp. The effect of the barrier height is illustrated in Fig. 4, where we vary the maximum value of Ω_2 to load a controllable proportion of atoms between the lower and the upper wells, formed by ω_3 and ω_1, respectively. Starting from a cloud of thermal atoms in the lowest shell, the RF components ω_1 and ω_2 are turned on adiabatically following a procedure similar to that described in Fig. 3, in which Ω_1 is ramped directly to its final value. Initially, few atoms possess sufficient energy to cross the high barrier that results from a small Ω_2, and minimal population redistribution between the wells occurs. Increasing Ω_2 to lower the barrier allows more atoms to populate the second well. At around $\Omega_2 = 2\pi \times 400$ kHz the barrier vanishes and the atoms distribute themselves across the broad single well formed by the three RF dressing frequencies as shown in Fig. 1(c). Finally, Ω_2 is decreased to raise the barrier and split the population distribution into two distinct wells, with the proportion reflecting any imbalance between the lowest energy of each well. Figure 4(a) illustrates a loading process that transfers 52% of the atoms into the well defined by ω_1. This could be corrected or exacerbated by adjusting either Ω_1 or Ω_3 to raise or lower the potential energy minimum of each well.

Figure 5 illustrates the atom density arising from two possible transport sequences. Keeping the lowest energies of each well approximately equal allows us to load the balanced double shell with approximately 75% efficiency in atom number, while deliberately mismatching these energies allows a full population transfer between the wells. Crucially, Fig. 5 also demonstrates the effect of the barrier amplitude on the positions of the two trapping wells that is shown in the calculated energy levels in Fig. 1: the ω_1 and ω_3 potential minima are drawn closer together as the barrier is lowered to form the broad single well.

The simple potential shaping schemes demonstrated here for three frequencies comprise single wells, a double well, and a flattened three-frequency well. We have also demonstrated a method of dynamic control that provides the intermediate stages for loading. This approach can be extended in a straightforward manner by applying additional dressing RFs.

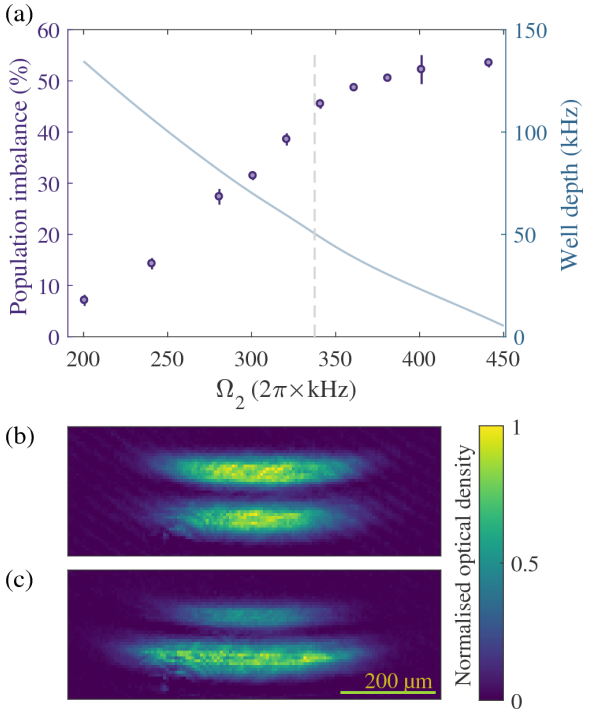

FIG. 4. (a) The percentage of atoms loaded from the wells formed by ω_3 to ω_1 for a given maximum amplitude of the ω_2 field, expressed in terms of $\Omega_2 = g_F \mu_B B_2/(\sqrt{2}\hbar)$ (purple circles). The RF amplitude ramps are qualitatively similar to Fig. 3, with $\Omega_1 = 2\pi \times 192$ kHz and $\Omega_3 = 2\pi \times 442$ kHz. This amplitude disparity compensates the effects of gravity, with a quadrupole gradient of $B_q^{'} = 154$ G cm^1. The barrier was ramped to its maximum value over 400 ms, then reduced to $2\pi \times 90$ kHz over 100 ms. The blue line shows the effective well depth (right-hand scale) seen by atoms in the well at ω_3 for each final value of Ω_2, and the dashed vertical line indicates the barrier height for which a separate well at ω_1 can no longer be resolved. (b, c) Absorption images of thermal atoms in the double shell at a quadrupole gradient of 60 G cm^{-1} after a 1-ms time of flight, with (b) an approximately balanced configuration with 52% of atoms in the upper shell and (c) 75% of the population in the lower shell. The color bar indicates the color map used for all absorption images in this work and has a linear scaling from 0 to the maximum optical depth in each image.

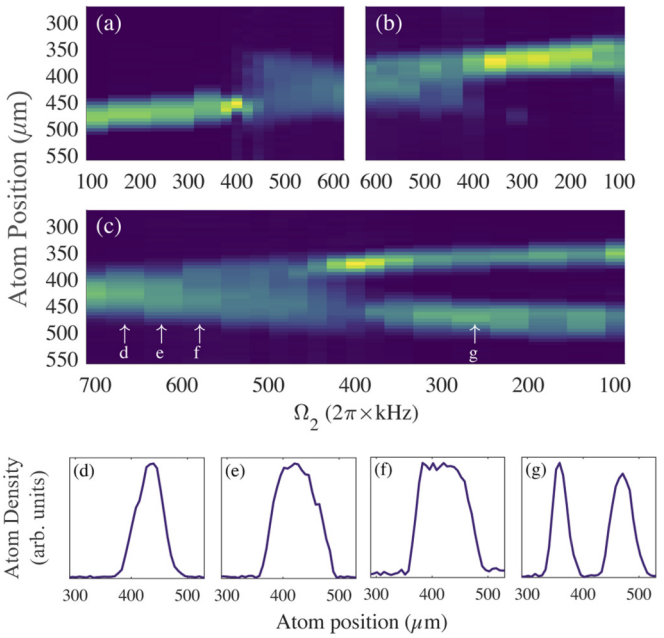

FIG. 5. (a–c) Vertical slices through in-trap absorption images of the MRF potential plotted vs the barrier amplitude Ω_2 and averaged over several experimental runs. Displacement is measured from the center of the quadrupole trap, and each slice scaled to the same total atom number. (a) All atoms begin in the shell at ω_3. With $\Omega_1 = 192$ kHz and $\Omega_3 = 446$ kHz, Ω_2 is ramped up (lowering the barrier) to flatten the potential and load the atoms into a broad single well. (b) Transport sequence with $\Omega_1 = 2\pi \times 192$ kHz and $\Omega_3 = 2\pi \times 511$ kHz. This tips atoms across the flattened 3-RF potential to load atoms from the lower to the upper shell upon reducing Ω_2 to raise the barrier. (c) Loading of a double-shell configuration from the flattened 3-RF potential, with $\Omega_1 = 2\pi \times 192$ kHz and $\Omega_3 = 2\pi \times 446$ kHz to maintain approximately equal atom populations in each well. The highest values of Ω_2 correspond to a single well, with two distinct wells forming as Ω_2 is reduced to raise the barrier. The apparent transfer of atoms into the shell at ω_1 around $\Omega_2 = 2\pi \times 400$ kHz is a normalization artifact, resulting from atom loss from the lower well due to technical noise in the apparatus. (d–g) Line plots of atom density for the snapshots in the double-shell loading sequence at barrier amplitudes labeled in (c) and corresponding to $\Omega_2 = 2\pi \times 660$ kHz (d), $\Omega_2 = 2\pi \times 622$ kHz (e), $\Omega_2 = 2\pi \times 577$ kHz (f), and, $\Omega_2 = 2\pi \times 266$ kHz (g). This shows the progression from 3-RF single well (d, e) to flat-bottomed 'box trap' (f) and double-shell potential (g).

C. RF spectroscopy

RF spectroscopy is an experimental technique commonly used to precisely characterize bare magnetic traps and adiabatic potentials [45,46]. A weak probe RF is applied to atoms held within the trap, causing expulsion of atoms when the probe RF is resonant with a transition between trapped and untrapped states. With these resonances appearing as dips in the measured atom number, the probe frequency is varied to map out the spectrum of transitions. For a BEC this resonance has a width of the order of the chemical potential (typically kilohertz), while for a thermal cloud the resonance is broadened due to the thermal distribution of atoms in the trap [46].

RF spectroscopy is employed here to characterize the key components of our trapping fields: the TOP field magnitude B_T, the amplitudes of applied dressing RF components, and, ultimately, the MRF eigenenergies. B_T is measured by RF spectroscopy of a condensate confined in the TOP, and $B_q^{'}$ calibrated by measuring the trap frequency of the center-of-mass mode of a condensate oscillating in this approximately harmonic potential at a known current through the quadrupole coils.

To calibrate the RF amplitudes, transition frequencies are measured for single-RF shells at $\omega_{1,2,3} = 2\pi \times (3,3.6,4.2)$ MHz. We use linearly polarized RF to measure the RF fields in the x and y directions independently. The Rabi frequencies are calculated from these measured resonances through Floquet

theory as described in Sec. II. This calculation incorporates the Bloch-Siegert shifts [47,48]. We also include the effect of gravity by adding the potential energy term $H_{\rm grav} = mgz$ to the Hamiltonian, Eq. (3), which typically shifts the transition by a few kilohertz. The amplitude of each RF component used in the MRF APs is deduced using a cowound pickup coil; we convert the measured voltage amplitudes into a magnetic field amplitude using the single-RF Rabi frequency calibration measurements. The linearity of the pickup coil response was verified by repeating the single-RF spectroscopy measurements for a variation in RF amplitude of up to 50%. We note that the combined MRF input approaches a value close to the saturation of the amplifier, resulting in a compression of the amplitudes of each RF component of up to 4% for the highest dressing RF powers applied; this saturation is accounted for by the RF pickup measurement.

The probe RF field must be sufficiently weak that it does not itself shift the transition. For the APs used here the Rabi frequencies of the dressing RFs are hundreds of kilohertz, while that of the probe is below 100 kHz. Selected RF spectroscopy measurements were repeated with probe amplitudes spanning 1/3 to 3 times their standard values, with no measurable shift of the resonance observed.

D. RF spectroscopy in the MRF potential

The closely spaced ladder of dressed-atom energy levels resulting from the application of multiple dressing RFs leads to a large number of transitions between different Floquet manifolds that can be driven by an appropriate probe RF field [32,49]. However, many of these correspond to higher-order multiple-photon processes with low transition rates. Determining the theoretical transition frequencies begins with the calculation of the AP eigenenergies using the Floquet method in Sec. II, followed by the selection of a single energy level corresponding to the double well from the infinite ladder of periodicity $\hbar\omega_f$. The condensate is localized at the position of minimum energy within the well near resonance with ω_1. Energy separations from this position in the trapped eigenstate to all untrapped eigenstates of the ladder are calculated, yielding a spectrum of possible transitions, but with no information as to the strength of each individual transition.

The calculated eigenenergies are experimentally verified using a BEC confined in the ω_1 shell, using a linearly polarized MRF field to minimize experimental variables and eliminate any experimental uncertainty arising from the phase between x and y field components. The spectroscopy method, calculated values, and measured results are illustrated in Fig. 6. We measure the dressed-state transition as illustrated in Fig. 6(a). By separately varying Ω_2 and ϕ_2, the amplitude and phase of the barrier RF, we experimentally probe the effects of these two parameters. These results are plotted in Figs. 6(c) and 6(d), respectively. The theoretical transitions were calculated for each set of measured RF field amplitudes Ω_j and phases ϕ_j and plotted with a finite width corresponding to the uncertainty arising from quadrupole gradient and RF amplitude calibrations.

The RF amplitude ramps for these measurements follow a method similar to that discussed in Sec. III A but starting with a BEC in the shell formed by the linearly polarized ω_1 field component, ramped from circular polarization over 500 ms. Ω_2 and Ω_3 are then ramped up to their final values with a set relative phase, to form the MRF potential in which RF spectroscopy is performed. For the barrier amplitude spectroscopy measurement plotted in Fig. 6(c), $\Omega_1 = 2\pi \times 187$ kHz and $\Omega_3 = 2\pi \times 248$ kHz, while Ω_2 takes values between 0 and $2\pi \times 332$ kHz with a quadrupole gradient $B_q' = 82.5$ G cm^{-1}. Over the course of the Ω_2 amplitude ramp, we measure a fall in Ω_1 by 5% and a rise in Ω_3 by 1% due to amplifier saturation and nonlinearities. This amplitude sweep is performed with a fixed phase relationship between the RF components, with relative phase components $\phi_{(1,2,3)} = (0, 0.302 \pm 0.001, 0.132 \pm 0.002)\pi$ radians, where the quoted uncertainty is given by the standard deviation of the measured relative phase of each RF component. The measured field amplitudes and relative phase values are accounted for in the calculated transition frequencies plotted as the theoretical gray line in Fig. 6. The phase variation measurement shown in Fig. 6(d) sees barrier amplitudes fixed at $\Omega_{1,2,3} = 2\pi \times (177, 310, 245)$ kHz, with $B_q' = 82.8$ G cm^{-1} and ϕ_2, the relative phase of the barrier component, varied over a π range. The amplitudes Ω_1 and Ω_3 are set such that the condensate remains confined to the initial well for the spectroscopy measurements, during which the weak RF probe is applied for a duration of 40 ms. The potential is deformed slowly to avoid sloshing of the condensate; ramps occur over a duration of 800 ms, which is slow compared to the inverse of the 200- to 400-Hz axial trap frequencies. The probe duration is sufficiently long that any residual sloshing in the wells would only manifest as a broadening of the measured RF spectroscopy resonances.

The resonance point is extracted from the asymmetric spectroscopy profile [46] by fitting a function of the form $a(x - b) + c/\sqrt{x - d}$. This function provides a good approximation to the asymmetric lineshape of the resonance profile, from which the resonant probe frequency that minimizes the atom number can be extracted. Only the data points lying within the range of the resonance were included in the fit, such that the asymmetric parabola captures the center of the resonance with minimal free parameters.

The actual lineshape can be simulated numerically [46] and is influenced by the amplitudes of both the dressing and probe RF fields and the chemical potential of the trapped condensate. With these factors, a separate fit for each spectroscopy data set is impractical and at risk of overfitting. Qualitative comparisons between the simulated lineshape and the chosen fit function suggest that the systematic uncertainty arising from a discrepancy between these models would be smaller than a kilohertz. The uncertainty in the fitted resonance location for both single-RF calibration and MRF potentials is estimated from the 99% confidence interval of the fitted minimum and is of order 1 to 3 kHz, although with a statistical accuracy limited by the sample size. This forms the dominant source of uncertainty in the measured transition frequencies, with a smaller influence from uncertainty in measuring dressing RF amplitudes with the pickup coils. Agreement is found with calculated values for the transition frequencies for both amplitude and phase measurements.

The total width of each MRF spectroscopy resonance is of order 10 kHz, with the peak itself identifiable to within 3 kHz. The 40-kHz shift of the resonance peak over the full

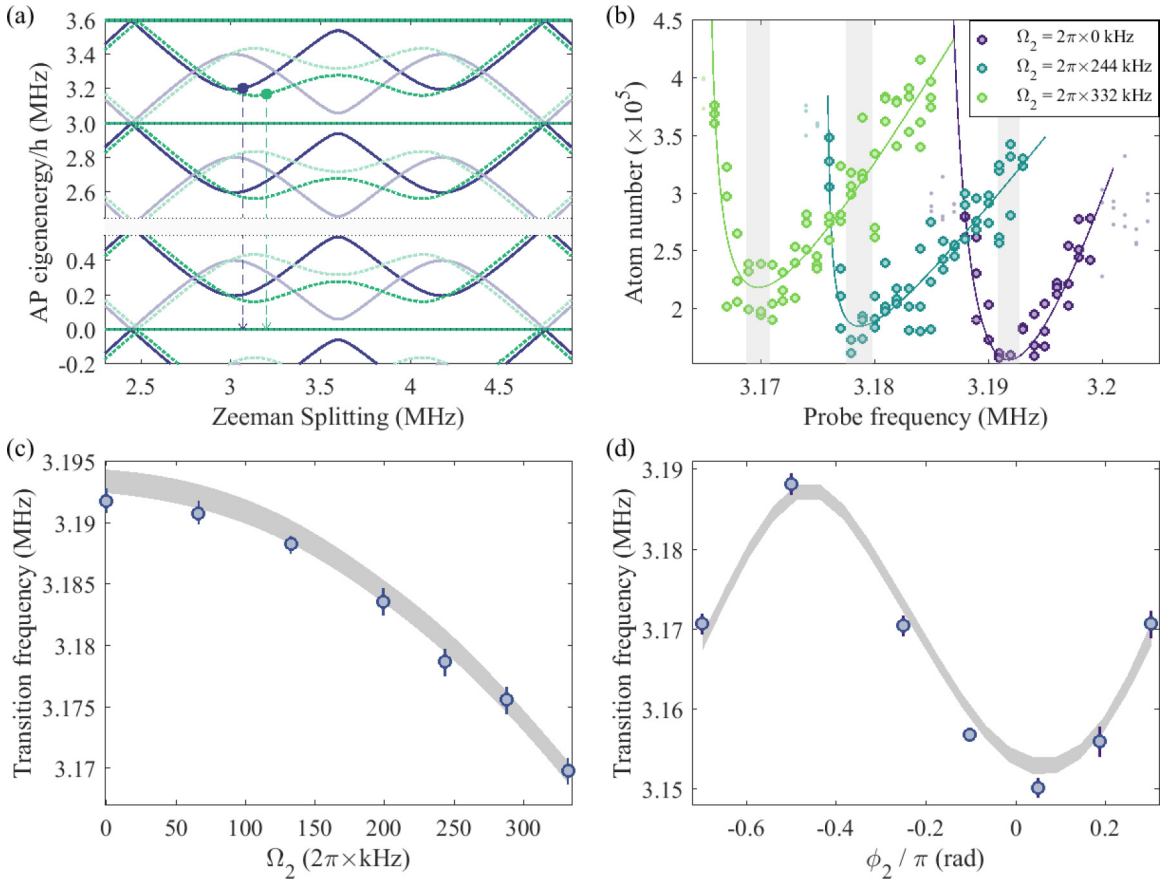

FIG. 6. (a) Sketch of the RF spectroscopy method showing dressed-state eigenenergies at two barrier heights, plotted in the absence of gravity. States corresponding to the two barrier heights are indicated by solid purple and dotted green lines. A BEC is confined in the well near ω_1, as illustrated by the circles, offset from the minima of the potential to incorporate gravity. We apply a probe RF resonant with the dressed-state transition, as illustrated by the arrows. (b) Measured spectroscopy resonances at $\Omega_2 = 2\pi \times 0$, $\Omega_2 = 2\pi \times 244$ kHz, and $\Omega_2 = 2\pi \times 332$ kHz, with $\Omega_1 = 2\pi \times 187$ kHz and $\Omega_3 = 2\pi \times 248$ kHz. Bold circles are included in the fit used to extract the minimum of the resonance (solid lines; see text), with gray sections indicating the 99% confidence interval for each minimum. (c) Change in measured (circles) and theoretical (line) resonances in the MRF potential for a range of values of Ω_2, corresponding to the full data set of the resonances shown in (b). The phase difference between RF components during this amplitude sweep was held constant, with relative phase values corresponding to the final circle in (d) with a barrier phase term $\phi_2 = 0.302\pi$ radians. (d) Change in measured (circles) and theoretical (line) resonances in the MRF potential for a range of values of ϕ_2 for fixed field amplitudes $\Omega_{1,2,3} = 2\pi \times (177{,}310{,}245)$ kHz. Error bars in both plots are calculated using the 99% confidence interval in the spectroscopy resonance fit in combination with the uncertainty in the RF amplitude and its calibration. The theory line was obtained with no free parameters by calculating the transition energy for each value of Ω_2 probed experimentally, with an interpolation between these values. Its finite width corresponds to the experimental uncertainty in the three measured RF amplitudes Ω_j at each value of Ω_2.

range of the parameter sweep is thus clearly resolved. The widths of each resonance are comparable to Ref. [45] although broader than those presented in Ref. [14]. This arises from the relatively weak vertical trap frequencies of 290 Hz in this work, compared to 2 kHz in Ref. [14], and the consequent increase in the broadening effect of the gravitational sag.

As shown in Fig. 6, increasing Ω_2 to lower the barrier reduces the energy separation between trapped and untrapped states for the measured transition. A shift in the measured RF spectroscopy resonance of the order of tens of kilohertz is observed as Ω_2 is varied, in agreement with the theory. The variation in transition energy with phase ϕ_2 relative to $\phi_{1,3}$, resulting from the dependence of nonlinear processes on the overall shape of the waveform, demonstrates a periodicity in π expected from the numerical calculations; the same calculations suggest that a 2π periodicity would arise upon varying ϕ_3.

IV. CONCLUSIONS AND OUTLOOK

We have performed the first experimental implementation of a multiple-RF adiabatic potential, using three separate dressing RFs to produce a double-well configuration with independent control over each trapping well and the barrier between them. We have demonstrated potential shaping through manipulation of the individual RF amplitudes, achieving transport from one well to another, a reliable loading sequence for this double well, and dynamic control over the barrier height. Experimental characterization of the MRF potential by RF spectroscopy of a trapped BEC validates the theoretical calculation of MRF eigenenergies by Floquet theory.

The separation of the wells in our scheme is determined by the quadrupole gradient and frequency spacing of the MRF components. In this work, we have demonstrated a large spacing, of order 100 μm.

This choice was motivated by the desire to image the double well *in situ* with a low-NA imaging system. Far smaller separations are possible using smaller frequency intervals and higher quadrupole gradients, limited only by the constraint that atoms follow the potential adiabatically [37]. For example, we have confined a BEC in a double well with a separation of 7.5 μm, using a frequency interval of 200 kHz, which is sufficient for matter-wave interference experiments. Exploiting the anisotropic character of RF dressed potentials [14], our technique could be used to probe the behavior of 2D systems [50]. Further reduction to a separation suitable for the observation of tunneling or Josephson oscillations is possible within the constraints imposed by adiabaticity.

Dressing with multiple independently generated radio-frequencies opens a range of new opportunities beyond the existing single-RF adiabatic potential experiments while retaining their characteristic smoothness and low heating rates. As an extension of this work, additional frequency components enable the implementation of more complex geometries such as lattices [19], box traps, and wells coupled to larger reservoirs. Independent control over both the polarization and the amplitude of each RF component permits further manipulations, for example, to connect our two trapping potentials at different locations through the spatial variation of the coupling strength. The MRF technique can also be combined with existing proposals to produce AP lattices using microstructured arrays of conductors [51,52] or provide a means of independent species-selective confinement for mixtures of atomic species with different g_F values [23].

ACKNOWLEDGMENTS

The authors would like to thank Rian Hughes for comments on the manuscript. This work was supported by EU H2020 Collaborative project QuProCS (Grant Agreement No. 641277). T.L.H., E.B., K.L., and A.J.B. thank the EPSRC for doctoral training funding.

[1] I. Bloch, J. Dalibard, and S. Nascimbéne, Nat. Phys. **8**, 267 (2012).
[2] P. Navez, S. Pandey, H. Mas, K. Poulios, T. Fernholz, and W. von Klitzing, New J. Phys. **18**, 075014 (2016).
[3] A. Ramanathan, K. C. Wright, S. R. Muniz, M. Zelan, W. T. Hill, C. J. Lobb, K. Helmerson, W. D. Phillips, and G. K. Campbell, Phys. Rev. Lett. **106**, 130401 (2011).
[4] F. Jendrzejewski, S. Eckel, N. Murray, C. Lanier, M. Edwards, C. J. Lobb, and G. K. Campbell, Phys. Rev. Lett. **113**, 045305 (2014).
[5] A. L. Gaunt, T. F. Schmidutz, I. Gotlibovych, R. P. Smith, and Z. Hadzibabic, Phys. Rev. Lett. **110**, 200406 (2013).
[6] L. Chomaz, L. Corman, T. Bienaimé, R. Desbuquois, C. Weitenberg, S. Nascimbène, J. Beugnon, and J. Dalibard, Nat. Commun. **6**, 6162 (2015).
[7] D. Husmann, S. Uchino, S. Krinner, M. Lebrat, T. Giamarchi, T. Esslinger, and J. P. Brantut, Science **350**, 1498 (2015).
[8] J. Choi, S. Hild, J. Zeiher, P. Schauss, A. Rubio-Abadal, T. Yefsah, V. Khemani, D. A. Huse, I. Bloch, and C. Gross, Science **352**, 1547 (2016).
[9] O. Zobay and B. M. Garraway, Phys. Rev. Lett. **86**, 1195 (2001).
[10] Y. Colombe, E. Knyazchyan, O. Morizot, B. Mercier, V. Lorent, and H. Perrin, Europhys. Lett. **67**, 593 (2004).
[11] J. Reichel and V. Vuletic, *Atom Chips* (John Wiley & Sons, New York, 2011).
[12] T. Schumm, S. Hofferberth, L. M. Anderson, S. Wildermuth, S. Groth, I. Bar-Joseph, J. Schmiedmayer, and P. Krüger, Nat. Phys. **1**, 57 (2005).
[13] M. Gring, M. Kuhnert, T. Langen, T. Kitagawa, B. Rauer, M. Schreitl, I. Mazets, D. A. Smith, E. Demler, and J. Schmiedmayer, Science **337**, 1318 (2012).
[14] K. Merloti, R. Dubessy, L. Longchambon, A. Perrin, P. E. Pottie, V. Lorent, and H. Perrin, New J. Phys. **15**, 033007 (2012).
[15] C. De Rossi, R. Dubessy, K. Merloti, M. de Herve, T. Badr, A. Perrin, L. Longchambon, and H. Perrin, New J. Phys. **18**, 062001 (2016).
[16] I. Lesanovsky and W. von Klitzing, Phys. Rev. Lett. **99**, 109901 (2007).
[17] M. Gildemeister, E. Nugent, B. E. Sherlock, M. Kubasik, B. T. Sheard, and C. J. Foot, Phys. Rev. A **81**, 031402(R) (2010).
[18] W. H. Heathcote, E. Nugent, B. T. Sheard, and C. J. Foot, New J. Phys. **10**, 043012 (2008).
[19] P. W. Courteille, B. Deh, J. Fortágh, A. Gunther, S. Kraft, C. Marzok, S. Slama, and C. Zimmermann, J. Phys. B **39**, 1055 (2006).
[20] S. Hofferberth, I. Lesanovsky, B. Fischer, J. Verdu, and J. Schmiedmayer, Nat. Phys. **2**, 710 (2006).
[21] M. Gildemeister, B. E. Sherlock, and C. J. Foot, Phys. Rev. A **85**, 053401 (2012).
[22] M. H. T. Extavour, L. J. LeBlanc, T. Schumm, B. Cieslak, S. Myrskog, A. Stummer, S. Aubin, and J. H. Thywissen, AIP Conf. Proc. **869**, 241 (2006).
[23] E. Bentine, T. L. Harte, K. Luksch, A. Barker, J. Mur-Petit, B. Yuen, and C. J. Foot, J. Phys. B **50**, 094002 (2017).
[24] N. R. Thomas, A. C. Wilson, and C. J. Foot, Phys. Rev. A **65**, 063406 (2002).
[25] T. G. Tiecke, M. Kemmann, C. Buggle, I. Shvarchuck, W. von Klitzing, and J. T. M. Walraven, J. Opt. B **5**, S119 (2003).
[26] I. Lesanovsky, T. Schumm, S. Hofferberth, L. M. Andersson, P. Krüger, and J. Schmiedmayer, Phys. Rev. A **73**, 033619 (2006).
[27] S. Hunn, K. Zimmermann, M. Hiller, and A. Buchleitner, Phys. Rev. A **87**, 043626 (2013).
[28] C. Cohen-Tannoudji and S. Haroche, J. Phys. **30**, 153 (1969).
[29] E. Muskat, D. Dubbers, and O. Schärpf, Phys. Rev. Lett. **58**, 2047 (1987).
[30] C. C. Agosta, I. F. Silvera, H. T. C. Stoof, and B. J. Verhaar, Phys. Rev. Lett. **62**, 2361 (1989).
[31] R. J. C. Spreeuw, C. Gerz, L. S. Goldner, W. D. Phillips, S. L. Rolston, C. I. Westbrook, M. W. Reynolds, and I. F. Silvera, Phys. Rev. Lett. **72**, 3162 (1994).
[32] H. Perrin and B. M. Garraway, Adv. At. Mol. Opt. Phys. **66**, 181 (2017).
[33] C. J. Foot, *Atomic Physics* (Oxford University Press, Oxford, UK, 2005).
[34] J. H. Shirley, Phys. Rev. **138**, B979 (1965).

[35] B. Yuen and C. J. Foot (unpublished) (2018).
[36] I. Lesanovsky, S. Hofferberth, J. Schmiedmayer, and P. Schmelcher, Phys. Rev. A **74**, 033619 (2006).
[37] K. A. Burrows, H. Perrin, and B. M. Garraway, Phys. Rev. A **96**, 023429 (2017).
[38] T. Morgan, T. Busch, and T. Fernholz, arXiv:1405.2534.
[39] A. Chakraborty and S. R. Mishra, arXiv:1703.03552.
[40] W. Petrich, M. H. Anderson, J. R. Ensher, and E. A. Cornell, Phys. Rev. Lett. **74**, 3352 (1995).
[41] Analog Devices AD9854.
[42] Mini-Circuits ZSC-2-2.
[43] Mini-Circuits LZY-22+.
[44] B. E. Sherlock, M. Gildemeister, E. Owen, E. Nugent, and C. J. Foot, Phys. Rev. A **83**, 043408 (2011).
[45] S. Hofferberth, B. Fischer, T. Schumm, J. Schmiedmayer, and I. Lesanovsky, Phys. Rev. A **76**, 013401 (2007).
[46] R. K. Easwaran, L. Longchambon, P.-E. Pottie, V. Lorent, H. Perrin, and B. M. Garraway, J. Phys. B **43**, 065302 (2010).
[47] F. Bloch and A. Siegert, Phys. Rev. **57**, 522 (1940).
[48] C. Cohen-Tannoudji and D. Guéry-Odelin *Advances in Atomic Physics: An Overview*, 1st ed. (World Scientific, Singapore, 2011).
[49] B. M. Garraway and H. Perrin, J. Phys. B **49**, 172001 (2016).
[50] L. Mathey and A. Polkovnikov, Phys. Rev. A **81**, 033605 (2010).
[51] G. A. Sinuco-León and B. M. Garraway, New J. Phys. **17**, 053037 (2015).
[52] G. A. Sinuco-León and B. M. Garraway, New J. Phys. **18**, 35009 (2016).